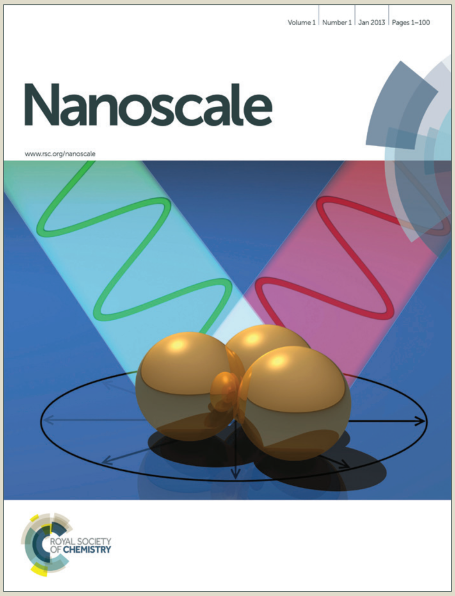

Morphology control, luminescence and energy transfer properties of $NaCeF_4$ and $NaCeF_4:Tb^{3+}/Yb^{3+}$ nanocrystals

Hongzhou Lian, Yunlu Dai, Dongmei Yang, Ziyong Cheng, Chunxia Li, Zhiyao Hou, Mengmeng Shang and Jun Lin *

State Key Laboratory of Rare Earth Resource Utilization, Changchun Institute of Applied Chemistry, Chinese Academy of Science, Changchun 130022, P.R. China

Abstract Oil-dispersible monodisperse $NaCeF_4$, $NaCeF_4:Tb^{3+}$ and $NaCeF_4:Yb^{3+}$ nanoparticles were prepared through a thermal decomposition method. The phase purity, morphology and luminescence properties were characterized by X-ray diffraction (XRD), transmission electron microscopy (TEM) and high resolution TEM (HRTEM), and photoluminescence (PL) spectra, respectively. The starting amount of NaF is crucial for phase purity, and the reaction time had an effect on the morphology of the products. Products with rectangles, rods, and their mixtures could be obtained at different reaction time. Under UV excitation, energy transfer from Ce^{3+} to lanthanide ions Tb^{3+} and Yb^{3+} could be observed in both $NaCeF_4:Tb^{3+}$ and $NaCeF_4:Yb^{3+}$. Energy transfer from Ce^{3+} to Tb^{3+} was proposed to be a resonant type (ET) by luminescent dynamic studies with theoretically calculated efficiency up to 93 %. Energy transfer from Ce^{3+} to Yb^{3+} was demonstrated as a cooperative (CET) process, and the CET efficiency and total theoretical quantum efficiency are 79 % and 158 %, respectively.

---

* Corresponding author. E-mail: jlin@ciac.ac.cn (Prof. Dr. Jun Lin)

1. Introduction

Shape and size-controlled synthesis and properties study of rare earth doped nano-fluorides have attracted much interest and attention recently, because of their dimension-dependent properties [1] and potential applications in optics [2], biological labeling [3], light emitting devices [4], and in enhancing the performance of solar cells [5]. Among these fluorides, $NaREF_4$ systems have been drawn particular attention, for their unique luminescent, ferromagnetic, magnetic, and piezoelectric properties [6]. Mai [6] et al. have demonstrated a general one-step synthesis route of dispersible α-$NaREF_4$ (RE: Dy, Ho, Er, Tm, Y, Yb, and Lu) and β-$NaREF_4$ (RE: Pr to Lu, Y) through the cothermolysis of $Na(CF_3COO)$ and RE-$(CF_3COO)_3$ in high-boiling solvent of oleic acid/oleylamine/1-octadecene for the first time. And from then on, luminescent materials based on $NaREF_4$ have aroused more and more interest mostly focused on upconverting materials [7]. However, few reports have been made on the investigation of $NaCeF_4$ system, partly because of the large cation radius of Ce^{3+}, and the difficulty to settle the cation into the lattice to get the crystalline compounds with large rare earth cations [8]. It is argued by Zeng et al. [9] that $NaCeF_4$ could be prepared by solvothermal method without synthesis detail described, however. Whereafter monodisperse CeF_3 and $NaCeF_4$ nanocrystals have been synthesized using the liquid–solid–solution (LSS) approach in the same group by Li et al. [10]. A detailed synthesis procedure by a polyolmediated solvothermal route with ethylene glycol (EG) as solvent for hexagonal monodisperse $NaCeF_4$ and $NaCeF_4$:Tb^{3+} nanorods have been also described by Qu et al. [8]. Other than these, there is no more report on study of nanoscaled $NaCeF_4$ particles, to the best of our knowledge.

On the other hand, because of the efficient energy transfer from Ce^{3+} to Tb^{3+} or Yb^{3+}, photoluminescence from Ce^{3+}, Tb^{3+} codoped materials [11] and downconversion from Ce^{3+} and Yb^{3+} couple in various hosts [12] have inspired much interest. As a sensitizer, Ce^{3+} ions possess some unique spectral properties, such as a broad UV absorption with a large cross-section due to allowed *4f–5d* transitions by Laporte parity selection rules, and a broad UV–blue emission band [11], which is advantageous to sensitize photoluminescence process for Tb^{3+} ions and downconversion process for Yb^{3+} ions. Photoluminescence properties of $NaCeF_4$:Tb^{3+} with doping concentration of 10 % have been reported by Qu et al. [8], but no detailed studies were performed. And there is no study on quantum cutting downconversion of $NaCeF_4$:Yb^{3+} system until now.

In this work, oil-dispersible monodisperse $NaCeF_4$ nanocrystals were prepared through thermal decomposition of NaF and RE-(oleate)$_3$ in high-boiling solvent of oleic acid/1-octadecene. Furthermore, we also prepared $NaCeF_4$:Tb^{3+} photoluminescence system and $NaCeF_4$:Yb^{3+} downconversion system and investigated their luminescent properties. The selection of Tb^{3+} as the downshifting couple for Ce^{3+} is not only for the green emission corresponding to $^5D_4$-$^7F_5$ transition, which favors enhancing spectral response of PV devices, but also the almost unity of quantum efficiency resulting from large gap to the lower $^7F_0$ level and absence of cross-relaxation between Tb^{3+} [8]. On the other hand, there is only one excited energy level in Yb^{3+} ($^2F_{5/2}$), and the simple energy level structure allows Yb^{3+} to exclusively absorb photons with energy of about 10000 cm^{-1} from other co-doped rare earth ions, such as Ce^{3+} and emit photons at ~980 nm, which can be absorbed by c-Si. The morphology and structure of $NaCeF_4$ doped with Tb^{3+} or Yb^{3+} were investigated, and furthermore, the photoluminescence properties of Tb^{3+} and quantum cutting downconversion characteristic of Yb^{3+} in $NaCeF_4$ nanocrystals were studied in detail, indicating their potential application for enhancing performance of PV solar cells.

2. Experimental

Chemicals. CeO_2 (99.99 %), Yb_2O_3 (99.99 %) and Tb_4O_7 (99.99 %) were purchased from Science and Technology Parent Company of the Changchun Institute of Applied Chemistry. Sodium oleate was purchased from Sinopharm Chemical Reagent Co., Ltd. Ethanol, n-hexane and cyclohexane were purchased from Beijing Chemical Regent Co., Ltd.. Oleic acid (OA) and 1-Octadecene (ODE) were purchased from Aldrich. All chemicals were used as received without further purification.

Preparation of rare earth oleate complexes. Rare earth oleate complexes were synthesized according to the literature method for the synthesis of iron-oleate complex [13]. Certain amount of rare earth oxides of CeO_2 (10 mmol), Yb_2O_3 (5 mmol) and Tb_4O_7 (2.5 mmol) containing 10 mmol of rare earth was dissolved in 5 ml of concentrated hydrochloric acid, respectively. Rare earth chlorides $RECl_3$ were obtained when hydrochloric acid was evaporated. The obtained chlorides and 30 mmol of sodium oleate were then dissolved in a mixture solvent composed of 20 mL of ethanol, 15 mL of distilled water, and 35 mL of hexane. The resulting mixture refluxes at 70 °C for 4 h. The upper organic layer was separated and washed with distilled water. After being washed, rare earth oleate complexes were procedure evaporating the remaining hexane.

Synthesis of oleic acid stabilized $NaCeF_4$, $NaCeF_4$: Tb^{3+} and $NaCeF_4$: Yb^{3+}. Following Chen et al. [14], oleic acid capped $NaCeF_4$, $NaCeF_4$: Tb^{3+}/Yb^{3+} were synthesized by thermal decomposition methodology. In a typical procedure for the preparation of $NaCeF_4$, 1 mmol of $Ce(oleate)_3$, 20 mmol of NaF, 10 mL of OA and 10 mL of ODE were added to the three-neck round-bottom reaction vessel and subsequently heated to 100 °C under a vacuum with magnetic stirring for 30min and flushed with N_2. The reaction was kept at 320 °C for 90 min in N_2 atmosphere under vigorous stirring. When the reaction was completed, the transparent yellowish reaction mixture was cool to 80 °C. The obtained $NaCeF_4$ was dispersed in 10 mL cyclohexane, precipitated with ethanol and gathered by centrifugation. The final sample was obtained by washing the precipitant three times and precipitated by centrifugation. $NaCeF_4$: Yb^{3+}/Tb^{3+} was prepared through the similar synthesis process, but doped with the rare earth ions Tb^{3+}/Yb^{3+}. The effects of NaF (8, 12, 16, 20, and 24 mmol), reaction time (90, 120 and 150 min) or doping concentration (Tb^{3+}, Yb^{3+}) on the morphology and size of the particles were investigated by changing the reaction condition of the three factors individually while the others remained constant as the typical route. $NaCeF_4$ with different doping concentration of Tb^{3+} (2, 4, 6, 8, 10 mol %) or Yb^{3+} (0.2, 0.4, 0.6, 0.8, 1.0, 1.2, 1.4, 1.6, 1.8, 2.0 mol %) were prepared through the similar procedure with the typical route except for the starting oleate. For example, $NaCeF_4$ doped with 1 mol % of Tb^{3+} (described as $NaCe_{0.9}F_4$:$0.1Tb^{3+}$) was prepared by adding 0.9 mmol Ce(oleate)$_3$ and 0.1 mmol Tb(oleat)$_3$ rather than 1 mmol Ce(oleate)$_3$ for $NaCeF_4$.

Instrument. Powder X-ray diffraction (XRD) patterns of the prepared powders were performed on a D8 Focus diffractometer (Bruker) with Cu Ka radiation (λ= 0.15405 nm) at a scanning rate of 6° min^{-1}. Samples for transmission electron microscopy (TEM) analysis were prepared by drying nanoparticle dispersion in hexane on amorphous carbon-coated copper grids. TEM and high-resolution transmission electron microscopy (HRTEM) images were obtained with an FEI Tecnai G2 S–Twin transmission electron microscopy with a field emission gun operated at 200 kV. The UV-VIS photoluminescence measurements were performed on a Hitachi F–7000 spectrophotometer equipped with a 150 W xenon lamp as the excitation source. The visible luminescence decay curves were obtained from a Lecroy Wave Runner 6100 digital oscilloscope (1 GHz) using a tunable laser (pulse width = 4 ns, gate = 50 ns, Continuum Sunlite OPO) as excitation source. Photoluminescence Quantum Yield (QY) was measured by absolute PL quantum yield measurement system C9920-02. The NIR photoluminescence spectra were studied by an FLS-920 spectrometer using a 450 W xenon lamp as the excitation source. The NIR photoluminescence decay spectra were obtained from the same instrument but using a 50W pulsed xenon lamp as the excitation source. All the measurements were performed at room temperature

3. Results and discussion

3.1 Sample Preparation

It has been noticed by Qu et al. [8] that morphology of nanoparticles prepared through solution-based procedure depends not only on the intrinsic crystal structure of the particle but also on the surroundings the crystal grows. Parameters, such as component and content of starting materials, reaction time, and medium in which crystal grows, are conditions that should be controlled for preparing high quality nanocrystals [15]. In this paper, a liquid-solid two-phase procedure was adopted to prepare oil-dispersible nanocrystals. 1-octadecene was chosen as the reaction medium for high temperature synthesis of nanocrystals for its high boiling point [14, 16] and oleic acid was chosen as capping agent to avoid clustering of particles and remain their dispersibility in oil. The effects of NaF content, reaction time and doping concentration on the phase and morphology of the particles were investigated.

NaF content. Here, NaF was used as both Na and F source for the preparation of $NaCeF_4$ nanocrystals. To investigate the effect of NaF amount as starting material on the phase of the final products, different NaF contents of 8, 12, 16, 20, and 24 mmol were selected, with amount of $Ce(oleate)_3$ fixed to 1 mmol. The structure of the prepared products was examined by XRD. The patterns of samples prepared with NaF amount of 8, 12, 16, 20, and 24 mmol are shown in Fig. 1 (a1), (a2), (a3), (a4), and (a5), respectively. When the starting amount of NaF is 8 mmol, no $NaCeF_4$ phase was detected from the XRD patterns, while a pure CeF_3 phase corresponding to JCPDS PDF NO. 08-0045 [in Fig. 1 (a1)] was obtained, indicating that $NaCeF_4$ phase cannot be formed under the condition of doubled the chemically stoichiometry of NaF. Hexagonal $NaCeF_4$ phase can be detected when the reaction started with 12 mmol of NaF accompanied with a certain amount of hexagonal CeF_3 phase as shown in Fig. 1 (a2), in which asterisk was used to denote diffraction peaks from CeF_3 phase in the mixture. As an unexpected phase, CeF_3 can also be observed when the starting amount of NaF is 16 mmol, as shown in Fig. 1 (a3). However, the amount of $NaCeF_4$ phase in the mixture of sample a3 is higher than that in sample a2. The relative amount of the $NaCeF_4$ in the mixture calculated from Whole Pattern Fitting and Rietveld Refinement is 68.0 wt % for the sample a2 and 78.6 wt % for the sample a3, while the calculated amount of CeF_3 phase for the two samples is 32.0 wt % and 21.4 wt %, respectively. Pure $NaCeF_4$ phase corresponding to JCPDS PDF NO.75-1924 listed at the bottom of Fig. 1b was obtained when the starting NaF amount increased to 20 mmol as shown in Fig. 1 (a4). Further increasing of NaF to 24 mmol can also induce the formation of pure $NaCeF_4$ as shown in Fig. 1 (a5). In summary, the experimental results showed that increased amount of NaF favored the formation of pure hexagonal $NaCeF_4$. These results indicate that NaF content is crucial in the formation of $NaCeF_4$ phase, which is agreement with that obtained by Qu et al. [8], when they studied the influence of NH_4F content on preparation of $NaCeF_4$ nanoparticles via a polyolmediated solvothermal route.

Reaction time. We also investigated the influence of the reaction time on the formation of $NaCeF_4$. Effect of reaction time on the structure and morphology of the products was examined by adjusting the reaction time by 90, 120, and 150 min with

$Ce(oleate)_3$ and NaF fixed at 1 mmol and 20 mmol, respectively. The as-prepared samples under the condition of 120 and 150 min were labeled as a6, and a7, respectively, and the sample prepared under 90 min, denoted as a4, as has been presented above. The XRD examination was performed to reveal the phase structure of the samples. The patterns of the samples are shown in Fig. 1a. It is shown from Fig. 1 (a4, a6, and a7) that all the samples have a hexagonal phase structure of $NaCeF_4$, and the prolonged reaction time has no significant influence on the phase purity of the final products. TEM images of the three as-prepared samples are illustrated in Fig. 2, which exhibit morphology of the sample a4, from which a great amount of hexagonal particles with uniform size of about 30 nm and a certain amount of rectangles with size of about 30 nm in length and 25 nm in width can be obtained. The TEM image observed with higher magnification (Fig. 2b) shows the smooth and flat surfaces of the particles. The uniformity and monodispersity of the hexagonal-shaped particles can also be indicated from the image with a certain number of rectangles observed. A further magnified TEM image shows polished arc angles of these rectangles with hexagons observed as shown in Fig. 2c. The structure of these hexagons and rectangles was examined by HRTEM. Fig. 2 d and h are the HRTEM images respectively corresponding to the rectangle and hexagonal particles, recorded from the cross section. A high crystallinity of the products is indicated from these images, and furthermore, it can be seen from Fig. 2d that only one kind of crystal lattice can be observed. The interplanar distances between adjacent lattice planes of about 0.308 nm is well coincident with the $(01\bar{1}1)$ plane of $NaCeF_4$. Two kinds of crystal lattice with interplanar distance of about 0.308 nm and 0.378 nm, corresponding to the neighboring $(01\bar{1}1)$ and (0001) planes, can be obtained from Fig. 3d. These results revealed that both the rectangle shape and the hexagonal shape of particles are single $NaCeF_4$ phase. In a word, monodisperse $NaCeF_4$ nanoparticles with dominant hexagonal shape can be achieved with this approach, which is in accordance to the result obtained from XRD examination as shown in Fig. 1a (sample a4). TEM images of the sample obtained after 120 min of reaction with other condition unchanged are shown in Fig. 2 (e-g). Unlike particles prepared under the condition of 90 min, the product consists of nanorods and a certain amount of hexagons. Nanorods of 80 nm in diameter and about 300 nm in length as well as hexagons with size of approximately 30 nm, can be seen more clearly from the highly magnified TEM images (Fig. 2 f and g). It can also be seen that hexagons are monodisperse beside the rods. Morphology of particles obtained after 150 min of reaction is exhibited in Fig. 2 i and j, from which it can be seen that almost all of the obtained products are rod-like with size about 100 nm in width and 450 nm in length, which is about 20 nm wider and 150 nm longer than those prepared under the condition of 120 min. The rod-like particles obtained can also be seen more clearly in the highly magnified TEM images, Fig. 2j. However, a further magnified image (Fig. 2k) reveals that non-rod shaped particles are remained after 150 min of reaction, although the amount of these particles is very small. A further investigation of Fig. 2k reveals the rod-like morphology of the samples.

Doping concentration. XRD and TEM examination are also used to investigate the effect of dopant on the structure and morphology of the products. Fig. 1b shows XRD patterns of $NaCeF_4$ with different dopants. $NaCeF_4$ doped with 2 and 10 mol % Tb^{3+} samples are denoted as sample b1 and b2, respectively. The products with 0.2 and 2 mol % Yb^{3+} doped is denoted as sample b3 and b4, respectively. All the diffraction peaks of these four samples can be exactly assigned to pure hexagonal phase of $NaCeF_4$ [space group: P321 (150)] with cell parameters of a=b=6.152 Å, c=3.777Å according to JCPDS PDF NO. 75-1924. No other phase or impurity can be detected, indicating that the Tb^{3+} or Yb^{3+} ions were completely dissolved in the $NaCeF_4$ host without inducing significant changes of the crystal phase even with high doping concentration (10 mol %) adopted in this study.

TEM images of $NaCeF_4$: 10 mol % Tb^{3+} and $NaCeF_4$: 2 mol % Yb^{3+} are exhibited in Fig. 3, denoted as a, b for sample b2 and c, d for sample b4, respectively. Highly uniform and monodisperse particles can be obtained from an overall view of images (Fig. 3 a and c). The smooth and flat surfaces of the particles can also be from the TEM images with higher magnification (Fig. 3 b and d). The results showed that size and morphology of doped particles were not significantly different from that of undoped ones, i.e., sample a4 mentioned above. The inserted HRTEM images in Fig. 3 b and d indicate the high crystallinity of doped nanoparticles. And furthermore, interplanar distances between adjacent lattice planes of about 0.308 nm is well coincident with the $(01\bar{1}1)$ plane of $NaCeF_4$. Briefly, the doping with Tb^{3+} or Yb^{3+} changes neither the crystalline phase nor the morphology of the matrix material.

Growth Mechanism. Fig. 2 (l) gives the schematic presentation of hexagonal-phase $NaCeF_4$ structures. In this hexagonal structure, two types of cation sites are presented by ordered array of F^- ions: one occupied by Na^+ and the other occupied randomly by Ce^{3+} and Na^+ [17]. The (1/3Ce^{3+}, 1/3Na^+) ions occupy sites with the 9-fold tricapped trigonal prism coordination, while the remaining sodium ions occupy sites with the 6-fold octahedral coordination. A crystal consists of a series of crystallographic planes, some of which are the surface planes and the others are the inner planes. For a hexagonal structure, as shown in Fig. 2 (l) , the surface planes contain the family of {0001} for top/bottom planes and the $\{10\bar{1}0\}$ **Error! Reference source not found.** family for side planes, and the side family consist of six energetically equivalent planes, i.e. $(10\bar{1}0)$, $(\bar{1}010)$, $(0\bar{1}10)$, $(01\bar{1}0)$, $(\bar{1}100)$, and $(1\bar{1}00)$ plane corresponding to the six side faces of the hexahedron [8, 18].

The formation of $NaCeF_4$ hexagonal was realized under the co-work of cation, i.e. Na^+, Ce^{3+} and anion, i.e. F^-, which compete with each other in the system. Due to the coordination effect between ions, cation and anion inevitably capped on crystal surfaces of $NaCeF_4$ unit cell, or {0001} plane family and the plane family of crystallography. The average number of dangling bonds on the crystal surface would be decreased by capping of F^-. And according to the Gibbs-Thompson theory, the relative chemical potential of a crystal is proportional to the ratio of the surface to atom, which is determined by the number of dangling bonds of the crystal [8]. Therefore, the total effect of F^- capping is to decrease the chemical potential of the crystal, and therefore decelerate the growth of nanocrystals. While the effect of anion capping works oppositely, Na^+ and Ce^{3+} favor the increasing of the crystal chemical potential, and therefore facilitate the growth of crystal. In this system, the concentration of positive ions, Na^+ and Ce^{3+} is higher than that of native ions, F^-, and consequently, depositing probability of the positive charges on the surface of crystal cell is higher than that of native charges. Therefore, it is thought that the total depositing speed of the positive charges of Na^+ and Ce^{3+} on the surface of crystal cell is higher than that of native charges of F^-. Therefore, the chemical potential would not decrease with the increasing concentration of F^- and the growth of the crystal would not be terminated by F^- as well. In a word, the positive charges of Na^+ and Ce^{3+} rather than F^- is dominant in this system. This is the reason why the nanocrystals of $NaCeF_4$ can be developed with the increasing F^- concentration, which decelerate the growth of nanocrystals.

On the other hand, we consider that under the lower NaF starting amount (lower than 12 mmol) condition, there would not be enough Na^+ and F^- capped on the surface of the monomers for formation of $NaCeF_4$, and as a result, only CeF_3 phase could be obtained. With increasing NaF amount, the capping concentration of sodium and fluorine increased, which facilitates the formation of $NaCeF_4$ nanocrystals. This result is agreement with what was observed by Qu et al. [8] using NH_4F as fluorine source $NaCeF_4$ nanocrystals. On the other hand, the capping effect of F^- on the {0001} crystal planes is greater than that on the $\{10\bar{1}0\}$ planes [8], and the capping probability of cations, Na^+ and Ce^{3+} on the top/bottom surface is also higher than the side planes because of coordination effect between anions and cations. Consequently, when the reaction time increased, nanocrystals grew faster along with the [001] orientation rather than with the other five orientations, i.e. [110], [011], [100], [010], and [210], as shown in Fig. 2(l), resulting the formation of nanorods.

3. 2 Photoluminescence Properties

$NaCeF_4$. Fig. 4a shows the excitation spectrum of Ce^{3+} *5d-4f* emission at room temperature in $NaCeF_4$ nanocrystals. It consists of one broad band ($\lambda_{max} \approx 260$ nm), which can be ascribed to *4f-5d* transition of Ce^{3+}. Splitting of *5d* orbital of Ce^{3+} can be clearly observed from the excitation spectrum in the region of 200-300 nm, resulting from the unique $4f^1$ electronic configuration of Ce^{3+}. Absence of electron in the *5s* and *5p* electron shells make electron in the inner *5d* orbital unshielded and exposed to the environment ions. And the *5d* orbital is the excited energy level for electrons promoted from ground state of 4f orbital under the excitation of UV photons. Therefore, splitting of the *5d* oriental can be observed macroscopically from the examination of excitation spectrum. On the other hand, given the fact that the corresponding transitions in the gaseous Ce^{3+} is peaked at about 200 nm, the ones in our sample are contrastively red-shifted about 60 nm. This can be attributed to the suppression of crystal field [8, 19]. Upon excitation into the Ce^{3+} band (λ_{ex}=260 nm) at room temperature, the emission spectrum is dominated by a Ce^{3+} *5d-4f* transition band with $\lambda_{max} \approx 360$ nm as shown in Fig. 4b. The Stokes shift has a value about 11000 cm^{-1}.

$NaCeF_4$:Tb^{3+}. Photoluminescence (PL) or luminescence downshifting is a process in which a substance absorbs photons (electromagnetic radiation) and then re-radiates photons. In the late 1970s, Hovel et al. proposed spectral down-shifter to overcome the poor spectral response of PV device to short-wavelength light [20]. Tb^{3+} is well–studied for its UV to visible downshifting properties [21] as mentioned above. On the other hand, the Ce^{3+} ion is a well-known sensitizer for trivalent rare earth ion and transition metal ion luminescence, and the sensitizing effects depend strongly on the host lattices into which these ions are introduced [22]. Down-shifting of UV photons to green emission resulted from energy transfer between Ce^{3+} and Tb^{3+} in various materials has been suggested potential application in enhancing efficiency of solar cells as well [5, 21].

Excitation spectra of $NaCeF_4$:Tb^{3+} nanoparticles with different doping concentration are shown in Fig. 5a. By monitoring the green emission of Tb^{3+}: $^5D_4$-$^7F_5$ transition (545 nm), the excitation spectrum consists of two different features in the UV-blue region, a broad and strong exciting band between 200 and 300 nm with peak around 260 nm, and some weak lines. The excitation lines between 300 and 500 nm are enlarged as inset in Fig. 5a, in which the detailed excitation peaks in this region are listed and assignment for these peaks is shown. The broad band can be ascribed to the *4f-5d* transitions of Ce^{3+} as has been discussed above in Fig. 4a, and the weak line comes from *f-f* transitions of Tb^{3+} ions [23], from which a favorable spectral overlap between Tb^{3+} excitation in the wavelength region of 300-500 nm and Ce^{3+} emission band as shown also in Fig. 4b can be verified. Furthermore, the presence of the Ce^{3+}

absorption band by monitoring emission of Tb^{3+} and the increased excitation intensity with increase of Tb^{3+} doping concentration suggest an energy transfer process from Ce^{3+} to Tb^{3+} [24]. The intensity of the *4f–5d* transition of Ce^{3+} is much stronger than that of the *f–f* transitions of Tb^{3+}. This can be attributed to the fact that the electronic transitions within the $4f^n$ configurations of the Tb^{3+} ions are strongly forbidden while the *4f–5d* transition of Ce^{3+} is electric-dipole-allowed.

Emission spectra upon excitation into Ce^{3+} *4f-5d* transition (λ_{ex}=260 nm) with different Tb^{3+} contents are shown in Fig. 5b. Both strong emission lines, ascribing to transitions of $^5D_4$ - ^7F_J (J = 3-6) Tb^{3+} ions and a broad band resulting from *5d-4f* transitions of Ce^{3+} can be observed. Corresponding assignments of energy level transition are listed in Fig. 5 as well. Compared to the excitation band, a Stokes shift of about 70 nm is observed for the Ce^{3+} *5d-4f* emission due to the vibration relaxation of the host. It can be observed from the figure that the emission intensity for Ce^{3+} decreased with increasing Tb^{3+} concentration, whereas the emission intensity for Tb^{3+} increases with increases of its concentration. This result can also indicate the occurrence of energy transfer process from Ce^{3+} to Tb^{3+} [25]. However, the presence of the Ce^{3+} emission band indicates that energy transfer from Ce^{3+} to Tb^{3+} is not complete. From Fig. 5 a and b, lower excitation strength and higher emission peaks of Ce^{3+} under lower doping concentration, indicated a smaller part of the excitation energy transferred from Ce^{3+} to Tb^{3+}. The larger average distance between these two ions at lower doping concentration is responsible for the less efficient energy transfer. The photograph of as-prepared $NaCeF_4$: $0.1Tb^{3+}$ nanoparticles dispersed in cyclohexane is shown in Fig. 5b as inset. High dispersibility of these particles in oil promoted formation of the transparent solution. Dissolution of nano-sized $NaCeF_4:Tb^{3+}$ particles can be attributed to functionalization of the particle surface by oleic acid ligands [5]. On the other hand, the photoluminescence and down-converting materials are generally placed on the front surface of a monofacial solar cell [5c], the transparency and stability of the photo-converting layer, fabricated by embedding optically active component into transparent matrix, are important factors for application of such kind of materials [5, 26]. The functionalized surface of the particles promotes compatibility of the particles with the matrix materials, and therefore favors the application of these materials for solar cells.

The energy transfer process between these two ions is thought to be a resonant energy transfer (ET) process, because the spectral overlap between the emission of the donor (Ce^{3+}) and the absorption of the acceptor (Tb^{3+}) is present [27]. Fig. 6 (left-hand side) illustrates the ET model for Ce^{3+}–Tb^{3+} in the host. Ce^{3+} ions can absorb UV light from the ground state ($^2F_{5/2}$) to the excited states, and then transfer the energy to the $^5D_3$ level of Tb^{3+} ions; subsequently, the $^5D_3$ level gives its characteristic transitions or relax to the $^5D_4$ level via cross relaxation. In this section, the room-temperature luminescent decay of Ce^{3+} and the ET mechanism between Ce^{3+} and Tb^{3+} will be discussed.

By investigating the decay curves of Ce^{3+}, the ET from Ce^{3+} to Tb^{3+} can be validated. As described by Blasse and Grabmaier [28], decay behavior of Ce^{3+} can be expressed by:

$$I = I_0 \exp(-t/\tau) \qquad (1)$$

where I and I_0 are the luminescence intensities at time t and 0, and τ is the luminescence lifetime. For samples of $NaCe_{1-x}F_4$: xTb^{3+} (x=0, 0.02, 0.04, 0.06, 0.08, 0.10), fluorescence decay curves by monitoring the Ce^{3+}: *5d-4f* transmission at 330 nm are shown in Fig. 7, and the lifetimes are bout 27.8, 27.2, 22.8, 22.5, 21.3, 20.9 ns, respectively. The lifetime in nanosecond order is the characteristic of the Ce^{3+} electric-dipole allowed *5d-4f* transition. Furthermore, the decrease of Ce^{3+} lifetime with increasing Tb^{3+} concentration can also be attributed to the ET process from Ce^{3+} to Tb^{3+}, where excited Ce^{3+} transferred energy to neighboring Tb^{3+}, causing decreased lifetime of itself, as has been described by Geng [25] and Huang [29]. ET from Ce^{3+} to Tb^{3+} can be further proved from the absolute quantum yield examination. The absolute quantum yields and CIE color coordinates of $NaCe_{1-x}F_4$: xTb^{3+} (x=0, 0.02, 0.04, 0.06, 0.08, and 0.10) under 260 nm UV excitation are summarized in Table 1, from which increase of absolute quantum yields in the visible region can be obtained with increase of Tb^{3+} concentration. The ET efficiency from Ce^{3+} to Tb^{3+} was also investigated. Generally, the ET efficiency from sensitizer to activator can be expressed by the following equation:[30,31]

$$\eta_T = 1 - \frac{I_S}{I_{S0}} \qquad (2)$$

in which I_S and I_{S0} are the luminescence intensities of the sensitizer (Ce^{3+}) with and without the activator (Tb^{3+}) , respectively. The calculated ET efficiency of with $NaCe_{1-x}F_4$: xTb^{3+} (x=0.02, 0.04, 0.06, 0.08, and 0.10) is about 85 %, 86 %, 88 %, 90 %, and 93 % respectively [25, 32].

Considering the dipole–quadrupole interaction between Ce^{3+} and Tb^{3+} ions [25, 29, 33], the critical distance (R_c) from the sensitizer to acceptor can be calculated with spectral overlap method, as expressed [34]:

$$R_C^8 = 3.024 \times 10^{12} \lambda_S^2 f_q \int \frac{F_S(E) F_A(E) dE}{E^4} \quad (3)$$

where f_q is the oscillator strength of the Tb^{3+} electric quadrupole transition, λ_S (in Å) is the wavelength position of the sensitizer's emission, E is the energy involved in the transfer (in eV), and $F_S(E)F_A(E)dE/E^4$ represents the spectral overlap between the normalized shapes of the Ce^{3+} emission $F_S(E)$ and the Tb^{3+} excitation $F_A(E)$. The value of f_q was suggested by Verstegen et al. that the ratio f_q/f_d is about 10^{-3} to 10^{-2}, where $f_d=10^{-6}$ is the oscillator strength of the Tb^{3+} electric dipole transition [35]. The calculated critical distance R_C of sample $NaCe_{0.9}Tb_{0.1}F_4$ with the dipole–quadrupole interaction method is 22.3–29.8 Å. Although this critical distance value is not very accurate, it indicates that the energy transfer can occur between Ce^{3+} and Tb^{3+} in a relatively long distance.

$NaCeF_4$:Yb^{3+}. Downconversion (DC) is a simultaneous energy transfer from an ion excited by photon (donor) to two neighbored ions (acceptors), each accepting half the energy of the absorbed photon. For solar cells application, Yb^{3+} is ideally suited because of the single excited state ($^2F_{5/2}$) approximately 10000 cm^{-1} above the ground state ($^2F_{7/2}$), corresponding to an emission around 980 nm. The simple energy level structure allows Yb^{3+} to exclusively absorb photons with energy of about 10000 cm^{-1} from other co-doped ions and emit photons at ~980 nm. Ce^{3+} is such kind of ion which can transfer the *4f-5d* transition energy to Yb^{3+} [36] by means of metal-to-metal charge transfer through redox reaction [37]. It has been realized by Trupke [26a] that downconverting materials can be used for increasing the efficiency of solar cells. A calculated efficiency of 38.6 % can be achieved by locating the downconverting materials on the front surface of a solar cell for solar cells with Eg=1.1 eV, a significant improvement over the 30.9 % which can be achieved with a conventional solar cell under the same assumption of only radiative recombination [38]. In this section, we stress emphases on the downconversion of $NaCeF_4$:Yb^{3+} nanoparticles. The excitation spectra of $NaCeF_4$: Yb^{3+} with various Yb^{3+} contents are shown in Fig. 8a. By monitoring $^2F_{5/2}$-$^2F_{7/2}$ transition of Yb^{3+} at 974 nm, a band centered at 260 nm assigned to the characteristic *4f–5d* transition of Ce^{3+} is observed. The presence of the Ce^{3+} absorption band suggests that there exists an ET process from Ce^{3+} to Yb^{3+}, as mentioned above. It can also be noted from the excitation spectrum that the intensity of Yb^{3+} exciting band first reaches a maximum at 1 mol % and then remarkably decreases when Yb^{3+} content is further enhanced. Emission spectra of samples are exhibited in Fig. 8b, which consist of two different features. The broad emission band between 300 and 500 nm with peak at about 360 nm is originated from the *5d-4f* transitions of Ce^{3+} and the other band in the range of 900 and 1100 nm peaking at 974 nm comes from *f-f* transitions of Yb^{3+} ions [36]. It is noticed that, as the Yb^{3+} content increases from 0 to 2 mol %, the luminescence of Ce^{3+} weakens monotonically, which can be attributed to the ET process from Ce^{3+} to Yb^{3+}. On the other hand, similar with that observed in the excitation spectra, the emission intensity of Yb^{3+} remarkably decreases with further-enhanced content after it reached a maximum at 1 mol % Yb^{3+} , which can be attributed to the concentration quenching between Yb^{3+} [36a]. High dispersibility of the $NaCeF_4$:0.01Yb^{3+} particles in oil can also be observed from the photograph of particle solution in cyclohexane as inset in Fig. 8a.

Because of the absence of the spectral overlap between emission of Ce^{3+} and absorption of Yb^{3+}, energy transfer from Ce^{3+} to Yb^{3+} is impossible to be a resonant process. On the other hand, as observed above, the emission energy of Ce^{3+} 5d energy level (~30000 cm^{-1}) is higher than twice of the absorption energy of Yb^{3+} $^2F_{5/2}$ energy level (~10000 cm^{-1}), implying a theoretical possibility of cooperative energy transfer (CET) from Ce^{3+} to Yb^{3+}, where one donor excites two acceptors simultaneously [27, 36a]. On the other hand, because of the observation of Ce^{3+} absorption when monitoring Yb^{3+} emission, and there is no levels of Yb^{3+} up to the UV region, the only possible route to achieve the Yb^{3+} NIR emission in this system is the relaxation of Ce^{3+}: *5d* - 2Yb^{3+}: $^2F_{5/2}$. Therefore, the energy transfer process is proposed to be a CET process, which is illustrated in Fig. 6 (right-hand side) as well.

The CET efficiency (η_{CET}) could be estimated by eqn. 2, in which I_S and I_{S0} are the integrated luminescence intensities of the sensitizer (Ce^{3+}) with and without the activator (Yb^{3+}) respectively, and furthermore, the theoretical maximum DC quantum efficiency (η_{QE}) could also be estimated by [39]:

$$\eta_{QE} = \eta_{Ce}(1-\eta_{CET}) + 2\eta_{Yb}\eta_{CET} \quad (4)$$

in which, η_{Ce} and η_{Yb} stand for the luminescent quantum efficiencies of Ce^{3+} and Yb^{3+}, respectively. η_{Ce} can be obtained from the absolute quantum yields measurement, and by assuming that all the excited Yb^{3+} ions decay radiatively, i.e., η_{Yb}=1, the upper limited values of the total DC quantum efficiency can be estimated. The measured $\eta_{Ce,}$ the calculated η_{CET}, and estimated η_{QE} with different Yb^{3+} content are listed in table 2. With increase in Yb^{3+} content from 0.2 to 2 mol %, both the CET efficiency and the DC efficiency increases monotonously, from 15 % to 79 % for η_{CET} , and from 44 % to 158 % for η_{QE}, respectively. However, quantum efficiency of Ce^{3+} emission within the range of 270 to 700 nm decreases with increase of Yb^{3+} ratio, from 20 % of undoped $NaCeF_4$ to 4 % of 2 mol % Yb^{3+} doped. The NIR decay curves for the Yb^{3+}: $^2F_{5/2}$-$^2F_{7/2}$ emission at 974 nm is plotted for the samples with various Yb^{3+} contents in Fig. 9. The Yb^{3+}:$^2F_{5/2}$-$^2F_{7/2}$ emission in the Yb^{3+} doped $NaCeF_4$ systems show a nearly single exponential decay, and the fitting yields a decay time of several milliseconds, which is the characteristics of the Yb^{3+} *f-f* transition. When Yb^{3+} content increases, the lifetime increases first and reaches its maximum to 3.26 ms at the doping concentration of 1 mol %. When Yb^{3+} content is further increased, the lifetime remarkably decreases, and drops down to 1.22 ms when the content increases to 2 mol %, as shown in the inset of Fig. 9. Corresponding to the decrease of emission intensity of with enhanced content of Yb^{3+}, the decrease of decay time decreased when its content was larger than 1.2 mol %, which can also be attributed to concentration quenching between Yb^{3+} [36a].

4. Conclusions

Oil-dispersible monodisperse $NaCeF_4$ and lanthanide (Tb^{3+} or Yb^{3+}) $NaCeF_4$

nanoparticles with well-defined shapes and good uniformity were prepared by a liquid-solid two-phase procedure. The phase and morphology of the as-prepared samples depend on the NaF content, reaction time and lanthanide dopant concentration. It is observed that the starting NaF content is an important factor for the phase-purity of the products, pure-phased $NaCeF_4$ could only be obtained with appropriate NaF content. Reaction time is a factor determining the morphology of the products. Both the phase purity and the morphology of the products remained unchanged with Tb^{3+} or Yb^{3+} doped in $NaCeF_4$. Upon excitation into Ce^{3+}, both photoluminescence of $NaCeF_4$: Tb^{3+} and downconversion of $NaCeF_4$:Yb^{3+} could be observed. Luminescent dynamics showed that downshifting between Ce^{3+} and Tb^{3+} achieved by a resonant ET process. And downconversion from Ce^{3+} to Yb^{3+} was demonstrated to be cooperative type (CET). All these results manifest that $NaCeF_4$ crystals are excellent host lattices for the luminescence of Tb^{3+} and Yb^{3+} ions. In a word, because of their unique luminescence properties and controlled morphology and size, these products may find potential applications for spectrum modification in PV devices.

Acknowledgements

This project is financially supported by the National Natural Science Foundation of China (NSFC 51172227, 51332008, 21221061), the National Basic Research Program of China (2010CB327704), and the Joint Funds of the National Natural Science Foundation of China and Guangdong Province (Grant No. U1301242)

References

1 A. P. Alivisatos, *Science*, 1996, **271**, 933.

2 J. W. Stouwdam, F. C. J. M. van Veggel, *Nano Lett.* 2002, **2**, 733.

3 (a) G. S. Yi, H. C. Lu, S. Y. Zhao, G. Yue, W. Yang, D. P. Chen, L. H. Guo, *Nano Lett.*, 2004, **4**, 2191; (b) Z. Gu , L. Yan , G. Tian , S. Li , Z. Chai , Y. Zhao, *Adv. Mater.*, 2013, **25**, 3758.

4 S. Sivakumar, F. C. J. M. van Veggel, M. Raudsepp, *J. Am. Chem. Soc.*, 2005, **127**, 12464.

5 (a) J. F. Suyver, A. Aebischer, D. Biner, P. Gerner, J. Grimm, S. Heer, K. W. Krämer, C. Reinhard, H. U. Güdel, *Opt. Mater.*, 2005, **27**, 1111; (b) Bryan M. van der Ende, Linda Aarts, Andries Meijerink, *Phys. Chem. Chem. Phys.*, 2009, **11**, 11081; (c) F. Wang and X. Liu, Chem. Soc. Rev., 2009, **38**, 976; (d) Wang H, Miroslaw Batentschuk , Andres Osvet , Luigi Pinna , and Christoph J Brabec, *Adv. Mater.*, 2011, **23**, 2675; (e) J. Chang, Y. Ning, S. Wu, W. Niu , S. Zhang, *Adv. Funct. Mater.*, 2013, **23**, 5910. (f) Z. Chen, H. Chen, H. Hu, M. Yu, F. Li, Q. Zhang, Z. Zhou, T. Yi, C. Huang, *J. Am. Chem. Soc.*, 2008, **130**, 3023.

6 H. Mai, Y. Zhang, R. Si, Z. Yan, L. Sun, L. You, C. Yan, *J. Am. Chem. Soc.*, 2006, **128**, 6426.

7 (a) H. Xu, L. Cheng, C. Wang, X. Ma, Y.G. Li, Z. Liu, *Biomaterials*, 2011, **32**, 9364; (b) Q. Liu, Y. Sun, C.G. Li, J. Zhou, C.Y. Li, T.S. Yang, X.Z. Zhang, T. Yi, D.M. Wu, F.Y. Li, *ACS Nano*, 2011, **5**, 3146; (c) D. Yang, X. Kang, M. Shang, G. Li, C. Peng, C. Li, J. Lin, *Nanoscale*, 2011, **3**, 2589; (d) Y. Dai, D. Yang, P. Ma, X. Kang, Y. Zhang, C. Li, Z. Hou, Z. Cheng, J. Lin, *Biomaterials*, 2012, 33, 8704-8713; (e) Y. Liu, D. Tu, H. Zhu, X. Chen, *Chem. Soc. Rev.*, 2013, **42**, 6924.

8 X. Qu, H. K. Yang, G. Pan, J. W. Chung, B. K. Moon, B. C. Choi, J. H. Jeong, *Inorg. Chem.*, 2011, **50**, 3387.

9 J. H. Zeng, Z. H. Li, J. Su, L. Wang, R. Yan, Y. Li, *Nanotechology*, 2006, **17**, 3549.

10 S. Li, T. Xie, Q. Peng, Y. Li, *Chem. Eur. J.*, 2009, **15**, 2512.

11 (a) Velázquez JJ, Rodríguez VD, Yanes AC, del-Castillo J, Méndez-Ramos J, *Opt. Mater.*, 2012, **34**, 1994; (b) D. B. He, C. L. Yu, J. M. Cheng, S. G. Li, L. L. Hu,

Chinese Phys. Lett., 2010, **27**, 114208.

12 (a) Q. H. Zhang, J. Wang, G. G. Zhang, Q. Su, *J. Mater. Chem.*, 2009, **19**, 7088; (b) J. Ueda, S. Tanabe, J. App. Phys., 2009, **106**, 043101; (c) H. Lin, S. M. Zhou, H. Teng, Y. K. Li, W. J. Li, X. R. Hou, T. T. Jia, *J. App. Phys*., 2010, **107**, 043107; (d) J. Chen, H. Zhang, F. Li, H. Guo, *Mater. Chem. Phys.*, 2011, **128**, 191; (e) S. W. Li, *Advanced Research on Material Engineering, Architectural Engineering and Informatization*, 2012, **366**, 215; (f) R. Zhou, X. T. Wei, S. Huang, Y. H. Chen, M. Yin, *J. Alloys Compd.*, 2012, **537**, 123.

13 J. Park, K. An, Y. Hwang, J. Park, H. Noh, J. Kim, J. Park, N. Hwang, T. Hyeon, *Nat. Mater.*, 2004, **3**, 891.

14 Y. Wei, F. Lu, X. Zhang, D. Chen, *Chem. Mater.*, 2006, **18**, 5733.

15 C. Li, J. Lin, *J. Mater. Chem.*, 2010, **20**, 6831.

16 J. Park, K. An, Y. Hwang, J. Park, H. Noh, J. Kim, J. Park, N. Hwang, T. Hyeon, *Nat. Mater.,* 2004, **3**, 891.

17 F. Wang, Y. Han, C. S. Lim, Y. Lu, J. Wang, J. Xu, H. Chen, C. Zhang, M. Hong, X. Liu, *Nature,* 2010, **463**, 1061.

18 C. Li, Z. Quan, J. Yang, P. Yang, J. Lin, *Inorg. Chem*. 2007, **46**, 6329.

19 R. Lang, Can. *J. Res.*, 1936, **14**, 127–130.

20 H. Hovel, R. Hodgson, J. Woodall, *Sol. Energy Mater. Sol. Cells*, 1979, **1**, 19-29.

21 (a) D. K. Yim, I. S. Cho, S. Lee, C. H. Kwak, D. H. Kim, J. K. Lee, K.S. Hong, *J. Nanosci. Nanotech*., 2011, **11**, 8748. (b) M. Sendova-Vassileva, D. Dimova-Malinovska, O. Angelov, J.C. Pivin, J. Optoelectron. *Adv. Mater.*, 2009, **11**, 1335; (c) W.Y. Zhang, Y.R. Ni, W.J. C.H. Huang, Lu, Z.Z. Xu, *J. Rare Earths,* 2010, **28**, 299-302.

22 G. G. Li, D. L. Geng, M. M. Shang, C. Peng, Z. Y. Cheng and J. Lin, *J. Mater. Chem.*, 2011, **21**, 13334.

23 Dorenbos, P. *Phys. Rev. B*, 2000, **62**, 15640.

24 C. X. Li, J. Yang, Z. W. Quan, P. P. Yang, D. Y. Kong, J. Lin., *Chem. Mater.* 2007, **19**, 4933.

25 D. Geng, G. Li, M. Shang, D. Yang, Y. Zhang, Z. Cheng, J. Lin, *J. Mater. Chem.*, 2012, **22**, 14262.

26 (a) T. Trupke, M. Green, P. Würfel, J. Appl. Phys., 2002, **92**, 1668; (b) T. Trupke, M. Green, P. Würfel, *J. Appl. Phys.*, 2002, **92**, 4117.

27 D. L. Dexter, *Phys. Rev.*, 1957, **108**, 630.

28 G. Blasse, B. C. Grabmaier, Luminescence Materials, Springer-Verlag, Berlin and Heidelberg, 1994, ch. 4–5

29 C. H. Huang, T. M. Chen, *J. Phys. Chem. C*, 2011, 115, 2349.

30 K. H. Kwon, W. B. Im, H. S. Jang, H. S. Yoo, D. Y. Jeon, *Inorg. Chem.*, 2009, **48**, 11525.

31 P. I. Paulose, G. Jose, V. Thomas, N. V. Unnikrishnan, K. R. M. Warrier, *J. Phys. Chem. Solids,* 2003, **64**, 841.

32 Z. Sun, Y. B. Li, X. Zhang, M. Z. Yao, L. Ma, W. Chen, *J. Nanosci. Nanotechn.*, 2009, **9**, 6283.

33 (a) N. Guo, Y. Song, H. You, G. Jia, M. Yang, K. Liu, Y. Zheng, Y. Huang, H. Zhang, *Eur. J. Inorg. Chem.,* 2010, 4636; (b) H.Y. Chung, C.H. Lu, C.H. Hsu, *J. Am. Ceram. Soc.*, 2010, **93**, 1838; (c) Rafael Martínez-Martínez, Enrique Álvarez, Adolfo Speghini, Ciro Falcony, Ulises Caldiño, *J. Mater. Res.*, 2010**, 25**, 484.

34 S. Nakamura and G. Fasol, The Blue Laser Diode, Springer, Berlin, 1996.

35 J. M. P. J. Verstegen, J. L. Sommerdijk, J. G. Verriet, *J. Lumin.*, 1973, **6**, 425.

36 (a) D. Chen, Y. Wang, Y. Yu, P. Huang, F. Weng, *J. App. Phys.*, 2008, **104**, 116105; (b) S.W. Li, *Advanced Research on Material Engineering, Architectural Engineering and Informatization*, 2012, **366**, 173; (c) R. Zhou, X.T. Wei, S. Huang, Y.H. Chen, M. Yin, *J. Alloys Compd.* 2012, **537**, 123; (d) J. Chen, H. Zhang, F. Li, H. Guo, *Mater. Chem. Phys.*, 2011, **128**, 191**.**

37 J. Ueda, S. Tanabe, *J. App. Phys.*, 2009, **106**, 043101.

38 H. Lian, Z. Hou, M. Shang, D. Geng, Y. Zhang, J. Lin, *Energy*, 2013, **57**, 270.

39 (a) R. T. Wegh, H. Donker, K. D. Oskam, A. Meijerink, *Science*, 1999**, 283**, 663; (b) P. Vergeer, T. J. H. Vlugt, M. H. F. Kox, M. I. Den Hertog, J. P. J. M. van der Eerden, A. Meijerink, *Phys. Rev. B*, 2005, **71**, 014119; (c) Q. Y. Zhang, C. H. Yang, Z. H. Jiang, X. H. Ji, *Appl. Phys. Lett.*, 2007, **90**, 061914; (d) S. Ye, B. Zhu, J. X. Chen, J. Luo, J. R. Qiu, *Appl. Phys. Lett.,* 2008**, 92**, 141112.

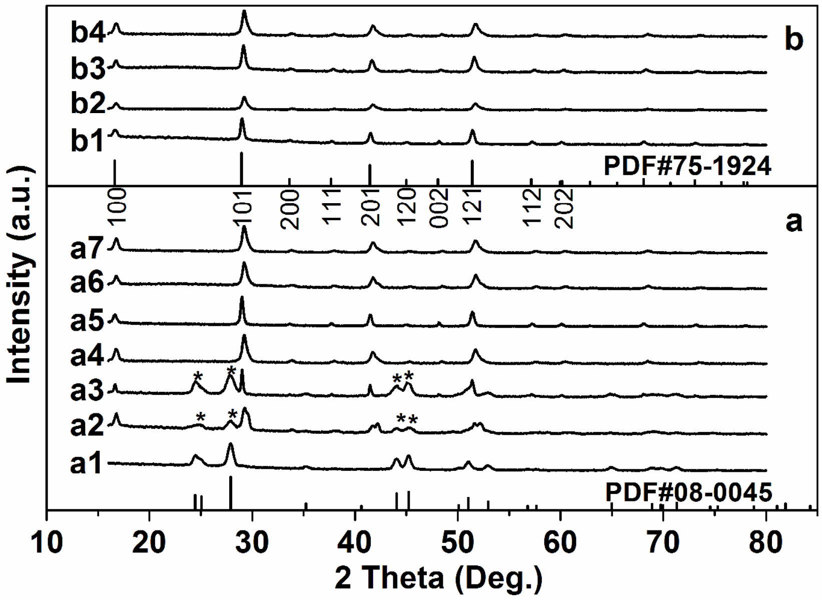

Figure1 XRD patterns of (a) samples synthesized with different NaF contents of 8, 12, 16, 20, and 24 mmol (a1-a5) and different reaction time of 120 and 150min (a6 and a7) and (b) as-prepared samples of 2, 10 mol % Tb^{3+} (b1, b2) and 0.2, 2 mol % Yb^{3+} (b3, b4) doped. The standard data of both $NaCeF_4$ (JCPDS no. 75-1294) and CeF_3 (JCPDS no. 08-0045) are listed as reference, and diffraction peaks from CeF_3 in the mixture are denoted as asterisks.

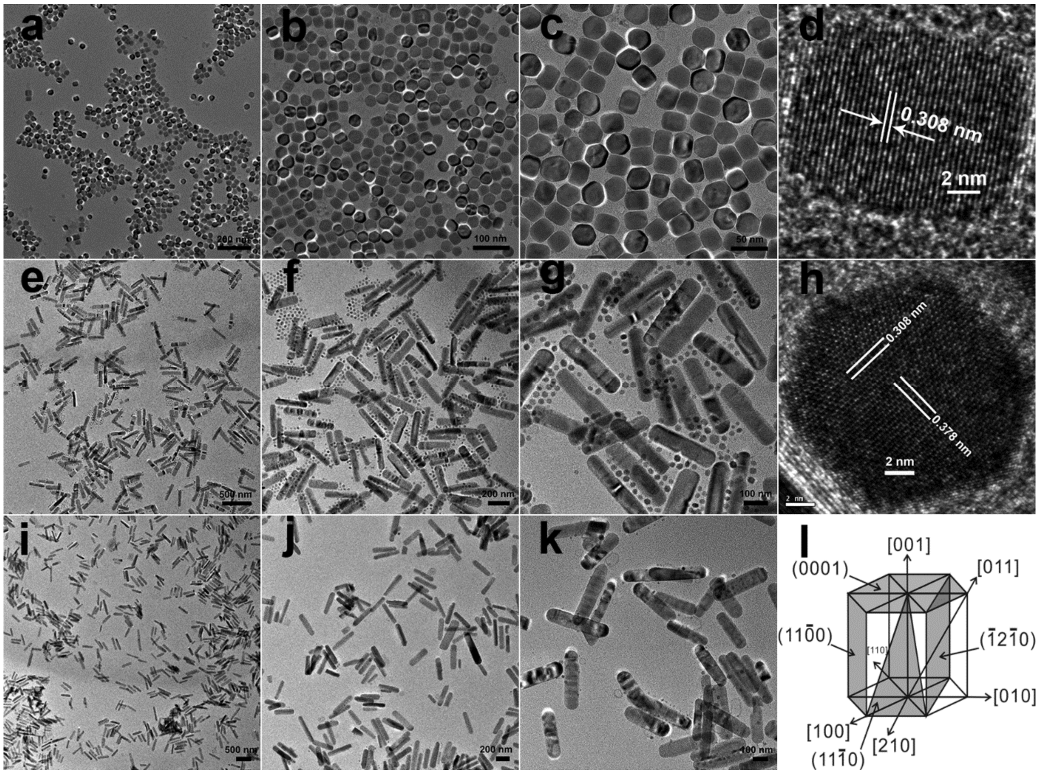

Figure 2 TEM images of $NaCeF_4$ samples prepared with different reaction time: (a-c) 90min, (e-g) 120min, (i-k) 150min. HRTEM of nanoparticles observed with rectangle (d) and hexagonal (h) shaped in (c) are also exhibited. (l) is schematic presentation of hexagonal-phase $NaCeF_4$ structures, with crystal orientations and some planes presented.

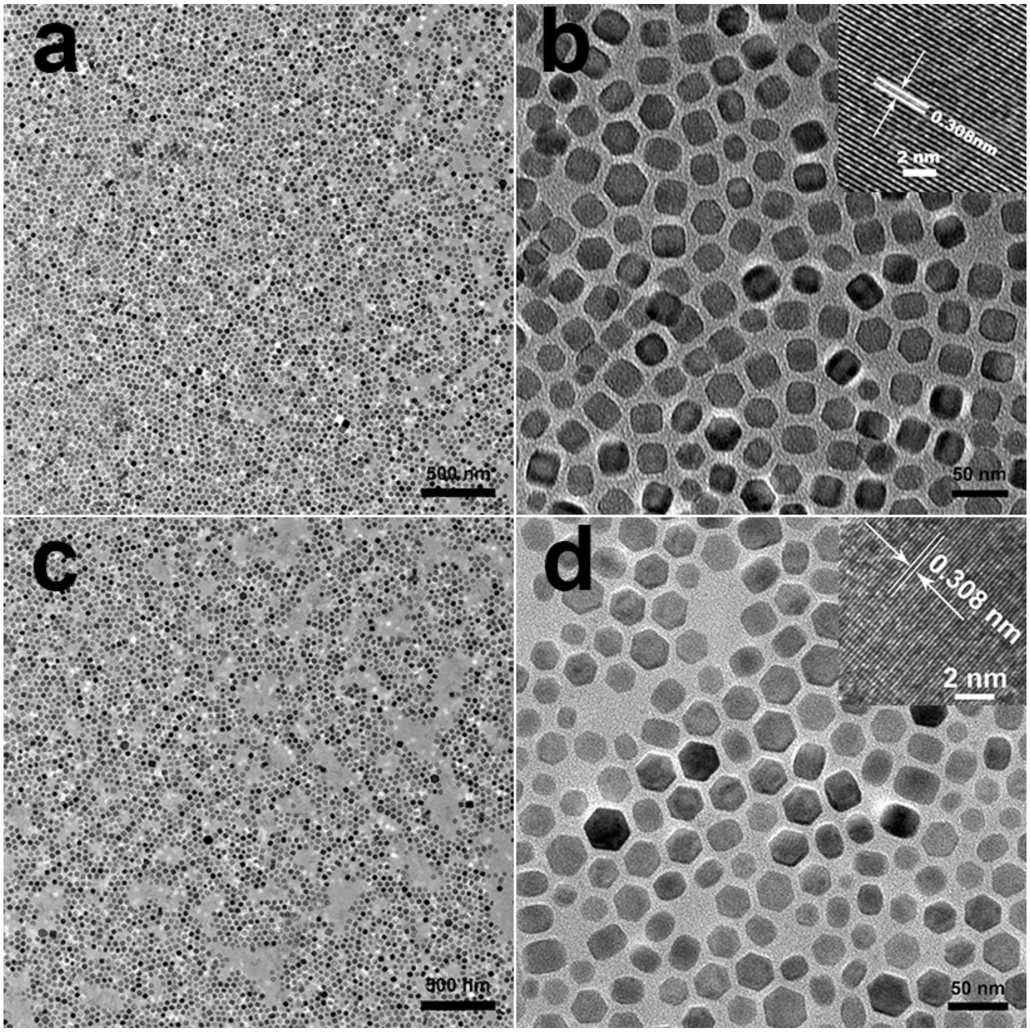

Figure 3 TEM images of $NaCeF_4$ samples doped with 10 mol % Tb^{3+} (a and b) and 2 mol % Yb^{3+} (c and d). The inset in b and d are HRTEM images from a single particle.

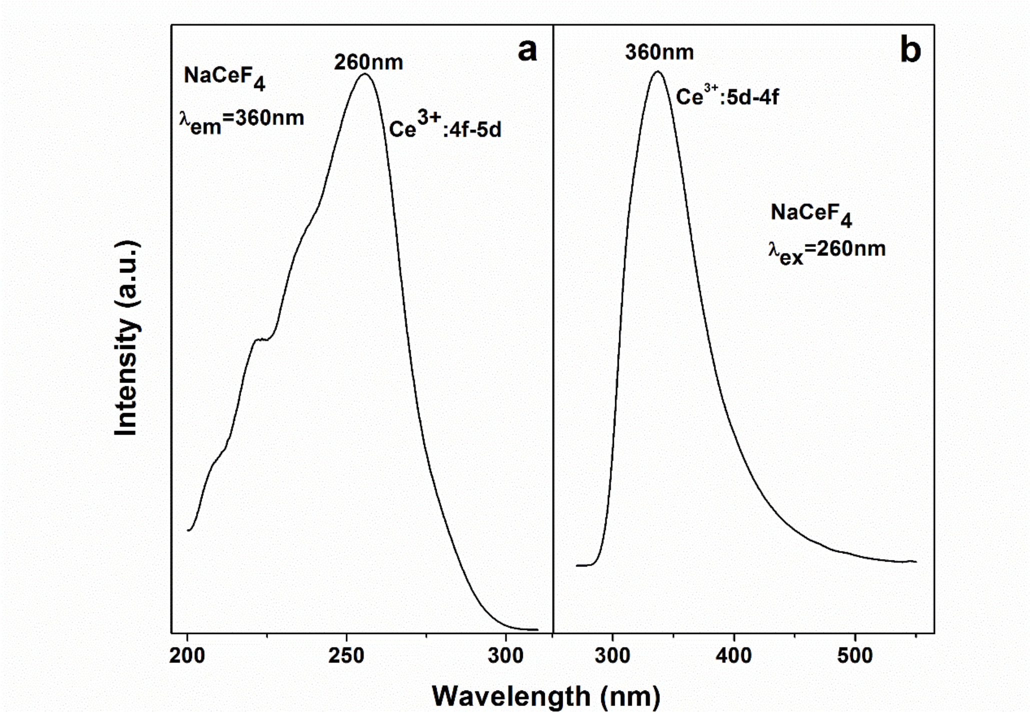

Figure 4 (a) Excitation spectrum of NaCe$_{1\text{-}x}$F$_4$ monitored at Ce^{3+} *5d-4f* emission (λ_{em}=360 nm); (b) Emission spectrum upon excitation into Ce^{3+} *4f-5d* transition (λ_{ex}=260 nm) for undoped NaCeF$_4$ nanoparticles at room temperature.

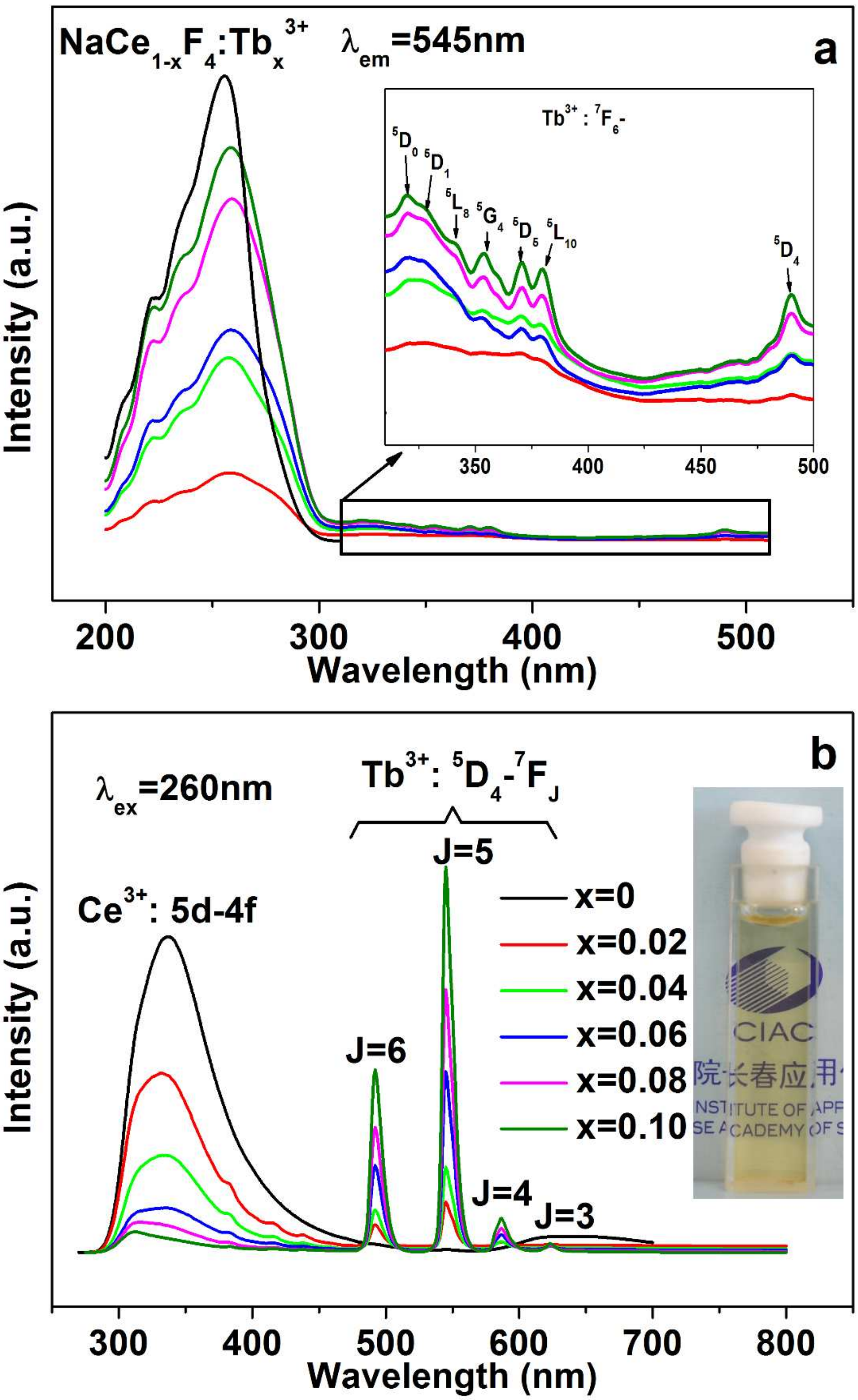

Figure 5 (a) Excitation spectrum of NaCeF$_4$:Tb^{3+} monitored at Tb^{3+} $^5D_4$-$^7F_5$ emission (λ_{em}=545 nm); (b) Emission spectrum upon excitation into Ce^{3+} *4f-5d* transition (λ_{ex}=260 nm) at room temperature. Representation in lines of various Tb^{3+} content is listed in (b). The inset in (a) shows the partly enlarged excitation spectrum of 300-500 nm, in which the assignment of Tb^{3+} excitation peaks is listed; the inset in (b) is the photograph of as-prepared NaCeF$_4$:Tb^{3+} nanoparticles in cyclohexane.

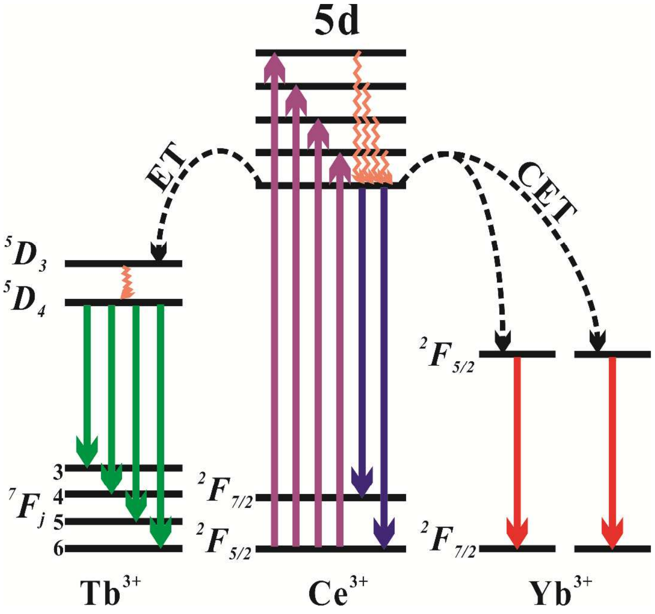

Figure 6 Illustration of the ET models for Ce^{3+}–Tb^{3+} (left part) and CET models for Ce^{3+}–Yb^{3+} (right part).

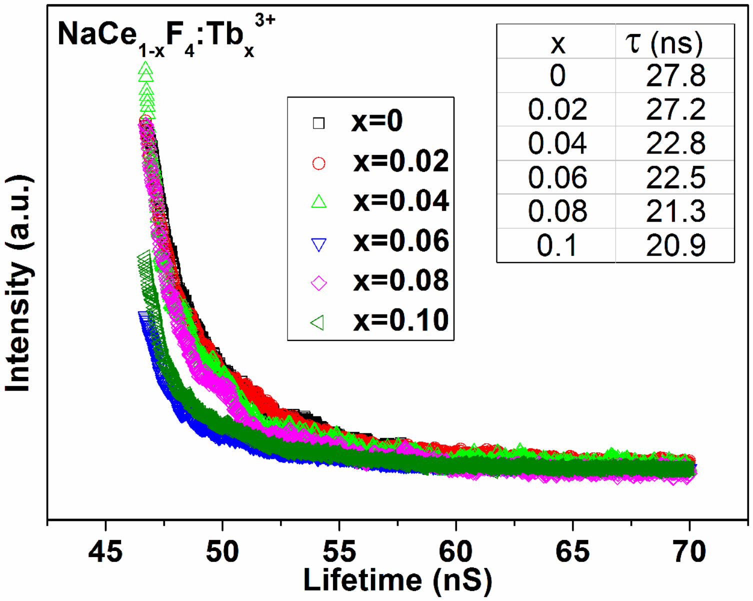

Figure 7 Luminescence decay curve of Ce^{3+}: 5*d*-4*f* transition under 260 nm of excitation in the samples with various Tb^{3+} contents. The inset shows the fitted lifetime of Ce^{3+} by single exponential decay.

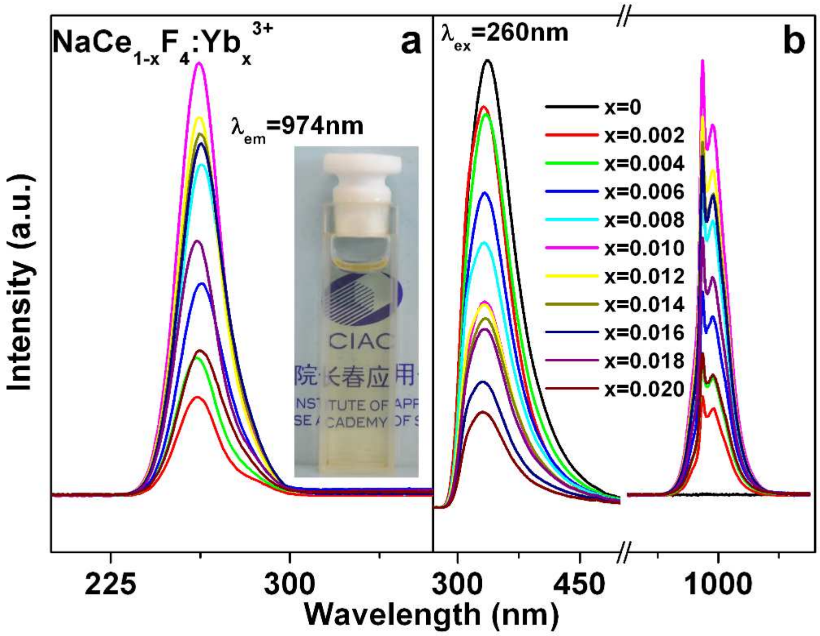

Figure 8 (a) excitation spectrum monitoring at Yb^{3+}:$^2F_{5/2}$-$^2F_{7/2}$ transition (λ_{em}=974 nm) and (b) emission spectrum upon excitation into Ce^{3+}: *5d-4f* transition (λ_{ex}=260 nm) of $NaCeF_4$:Yb^{3+} with various Yb^{3+} contents at room temperature. Representation of lines with various Yb^{3+} contents is listed in (b). The inset in (a) is the as-prepared $NaCeF_4$:Yb^{3+} nanoparticles in cyclohexane.

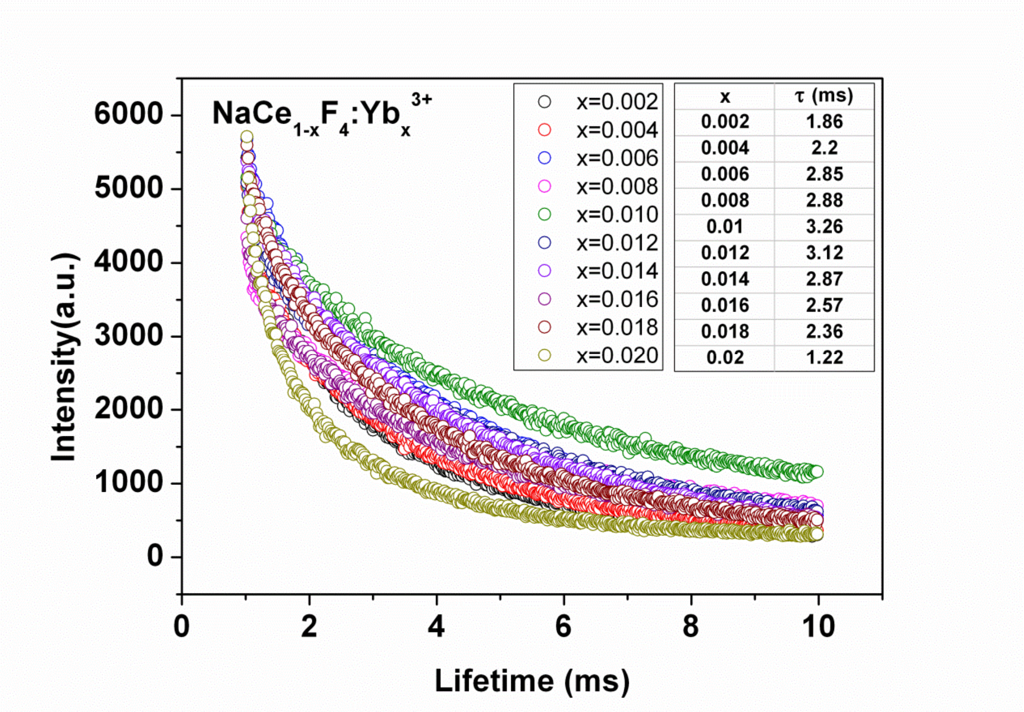

x	τ (ms)
0.002	1.86
0.004	2.2
0.006	2.85
0.008	2.88
0.01	3.26
0.012	3.12
0.014	2.87
0.016	2.57
0.018	2.36
0.02	1.22

Figure 9 Decay curves for the Yb^{3+}: $^{2}F_{5/2}$-$^{2}F_{7/2}$ transition in the $NaCe_{1-x}F_4$:xTb^{3+} samples with various Yb^{3+} contents under 260 nm excitation. The inset shows the fitted lifetime of Yb^{3+} by single exponential decay.

Table 1 Quantum yields and chromaticity coordinates (x, y) of $NaCe_{1-X}F_4$:xTb^{3+} samples under UV excitation (λ_{ex}=260 nm)

x	Quantum yields (%)	CIE coordinates (x, y)
0	22	0.235,0.193
0.02	16	0.321,0.534
0.04	22	0.318,0.551
0.06	29	0.325,0.569
0.08	30	0.329,0.577
0.10	31	0.332,0.585

Table 2 Quantum efficiency of Ce^{3+} (η_{Ce}), *CET* efficiency (η_{CET}) and the total theoretical quantum efficiency (η_{QE}) for $NaCe_{1-x}F_4$:xTb^{3+} samples with various Yb^{3+} contents

x	η_{Ce} (%)	η_{CET}(%)	η_{QE}(%)	x	η_{Ce}(%)	η_{CET}(%)	η_{QE}(%)
0	20	0	0	0.012	8	54	145
0.002	17	15	44	0.014	7	72	146
0.004	14	17	45	0.016	6	74	149
0.006	13	33	74	0.018	5	75	151
0.008	9	41	132	0.02	4	79	158
0.01	8	44	133				

TOC

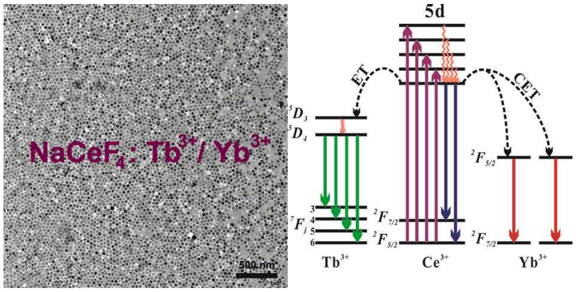

Growth mechanism and photoluminescence properties of $NaCeF_4$:Tb^{3+}/Yb^{3+} nanocrystals have been investigated for potential application of enhancing efficiency of solar cells.